ACS OMEGA

http://pubs.acs.org/journal/acsodf

Article

Facile and Green Synthesis of Novel Fluorescent Carbon Quantum Dots and Their Silver Heterostructure: An *In Vitro* Anticancer Activity and Imaging on Colorectal Carcinoma

Snehasis Mishra, Kaustav das, Sujan Chatterjee, Panchanan Sahoo, Sudip Kundu, Mrinal Pal, Asim Bhaumik, and Chandan Kumar Ghosh*

Cite This: *ACS Omega* 2023, 8, 4566−4577

Read Online

ACCESS | Metrics & More | Article Recommendations

ABSTRACT: Carbon dots (CQDs) have been widely investigated as prime candidates for developing a tumor theranostic platform due to their tunable fluorescence emission and excitation, high water solubility, good photostability, and biocompatibility. Among the CQDs, natural CQDs are an emerging class of nanomaterials in the carbon family. Herein, highly fluorescent carbon quantum dots (CQDs) were synthesized from orange juice using a one-step hydrothermal method and characterized by different techniques. After that, CQD/Ag heterostructures were synthesized by the reduction of silver salt, in particular silver nitrate ($AgNO_3$) solution using sodium borohydride ($NaBH_4$) in different ratios. The photostability and characterization of CQD/Ag heterostructures were investigated. At last, a comparative cellular toxicity measurement was done to select the superior CQD/Ag heterostructure in the human colorectal carcinoma (HCT 116) cell line along with the imaging property. The detailed cell death signaling was also observed in the HCT 116 cell line via the ROS-dependent mitochondrial-mediated pathway, where Akt (RAC-α serine/threonine-protein kinase) played a important role.

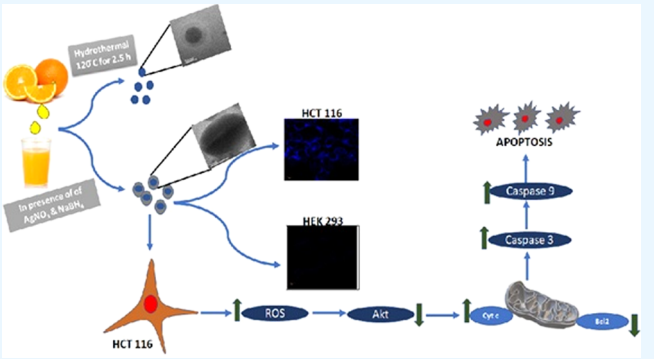

1. INTRODUCTION

Colorectal carcinoma is the most recurrent variety of primary colon cancer and is noted as the third most fatal type of cancer with a high mortality rate after lung and breast cancer.[1] A few decades ago, colorectal cancer was very uncommon or infrequently diagnosed.[2] Surprisingly, it is the world's fourth most deadly cancer now and is responsible for nearly about 900,000 deaths annually.[3] Besides, the dietary habits of developed and developing countries, obesity, lack of physical exercise, smoking, and harsh life style are major causative factors for colorectal cancer.[4] Improvements in pathophysiological understanding have enhanced the array of treatment options like endoscopic and surgical local excision, downstaging preoperative radiotherapy and systemic therapy, extensive surgery for locoregional and metastatic disease, local ablative therapies for metastasis, palliative chemotherapy, targeted therapy, immunotherapy etc.[5] Even though all of these new therapeutic approaches have doubled the overall survival rate, the survival is limited for nonmetastasized disease.

Different carbon-based nanomaterials are among the most dynamic fields in recent advanced materials science and engineering.[6,7] To date, many carbon nanomaterials such as fullerenes,[8] graphene,[9] carbon nanotubes,[10] graphene oxides,[11] carbon dots,[12] and carbon diamonds[13] have been synthesized and reported by various researchers. Among these, CQDs have become interesting because of their exceptional chemical and physical properties such as thermal and electrical conductivity, high mechanical strength, and their unique optical and fluorescence features.[14,15] They have been used in bioimaging, drug delivery, nucleus targeting and labeling, photodynamic therapy, optoelectronics, solar cells, photocatalyst design, photodetectors, and many other biological and engineering fields.[16]

Natural carbon-based quantum dots are an emerging class of nanomaterials in the carbon family. They have gained immense acclamation among researchers because of their abundance, eco-friendly nature, aqueous solubility, diverse functionality, and biocompatibility when compared to other conventional CQDs. There are various reports on different natural CQDs' synthesis and their different applications (Table 1). In the

Received: August 4, 2022
Accepted: November 18, 2022
Published: January 27, 2023

https://doi.org/10.1021/acsomega.2c04964
ACS Omega 2023, 8, 4566−4577

Table 1. Available Reports on Natural CQDs with Synthesis Procedure and Size

s. no	CQDs	synthesis methods	size (nm)	ref
1	white flowering plant	hydrothermal, 250 °C, 4 h	5	25
2	ascorbic acid	hydrothermal, 180 °C, 12 h	4.5	26
3	orange juice	hydrothermal,120 °C, 150 min	1.5−4.5	27
4	carrot roots	hydrothermal, 170 °C, 12 h	2.3	28
5	papaya	hydrothermal, 200 °C, 5 h	20	29
6	pomelo peels	hydrothermal, 220 °C,2 h	3	30
7	curcumin	hydrothermal, 180, 1 h	1.6	31
8	tulsi leaves	hydrothermal, 200 °C, 4 h	5	32
9	lemon juice	hydrothermal, 120−280 °C, 12 h	12−15 (200 °C), 3−5 (280 °C)	33
10	egg yolk oil	hydrothermal, 200 °C,60 min	10	34
11	chitosan	microwave, 450 W, 5 min	20	35
12	sucrose	microwave, 100 W, 3 min 40 s	3−10	36
14	lotus root	microwave, 800 W, 6 min		37
15	konjac flour	pyrolysis, 470 °C, 1.5 h		38
16	curcumin	pyrolysis, 180 °C	2−8	39
18	*aloe vera*	pyrolysis, 160−250 °C		40
19	raw cashew gum	microwave, 800 W, 30−40 min	9	41
20	fruit juice (kiwi, pear, avacado)	ultrasonic,30 °C, hydrothermal treatment 200 °C for 12 h	4.42 ± 0.05, 4.35 ± 0.04, 4.12 ± 0.03	42
21	neem leaves	chemical oxidation	5−6	43

present study, orange juice (OJ) was used as an exclusive reducing and stabilizing agent for the synthesis of nanoparticles.[17] On a molecular level, citric juices are composed of organic acids, phenolic compounds, and sugars that are able to reduce metallic ions to their elemental form.[18] While the main organic acids are malic, citric, and ascorbic, the most important sugars are glucose, sucrose, and fructose. Besides, there are between 10 and 15 phenolic compounds in these juices, including flavanones and hydroxycinnamic acids, which can serve as reducing agents.[19,20]

Nowadays, naturally occurring phytochemicals and secondary metabolites are widely used in therapeutics due to their specificity and tissue-protective nature.[21] In recent times, available reports have suggested that CQDs exhibit anticancer potential in various types of cancer.[22] There are also some reports that have demonstrated that silver nanoparticles have anticancer potential.[23] To achieve tumor-specific imaging and anticancer potential, carbon quantum dots were engineered by conjugating silver and phytochemicals.[24]

Herein, we develop highly fluorescent CQDs from orange juice (*Citrus nobilis deliciosa*), followed by a one-step hydrothermal method. This mechanism mainly involves the carbonization of sucrose, glucose, fructose, citric acid, and ascorbic acid, which are the leading constituents of orange juice. The synthesized carbon quantum dots are further used for creating the carbon quantum dot/silver heterostructure. The anticancer property of the CQD/Ag heterostructure was evaluated in the colorectal cancer (HCT 116) cell line. The fluorescence property of the heterostructure was also used for the bioimaging purpose.

2. EXPERIMENTAL SECTION

2.1. Chemicals for Synthesis. 2-Propanol (99% pure) was procured from Merck Life Science Private Limited, India. Sweet lime was bought from the local market. Pulp-free lemon juice was used as a carbon source for CD synthesis. For the carbon dot/silver heterostructure, we used silver nitrate ($AgNO_3$) as the silver source, and for reducing it to Ag nanoparticles, sodium borohydride ($NaBH_4$). Other chemicals were of analytical grade and all of the chemicals were used as received with purification.

2.2. Synthesis of Carbon Quantum Dots (CQDs) from Orange Juice (OJ). Freshly bought oranges from the local market were crushed and the juice was extracted. The seeds were carefully isolated and a thick juice was obtained. Then, the juice was centrifuged for approximately 6 min at 4000 rpm to extract the less-thick part of the juice. After that, 30 mL of the less-dense pulp-free lemon juice was mixed with 50 mL of 2-propanol to form a transparent solution. Then, the mixture was heated at 120 °C for 2.5 h in a solvothermal oven. After the reaction was completed, the oven was cooled down naturally to room temperature and a brown solution was obtained for further characterization. The hydrothermal synthesis of CQDs from naturally collected orange was executed at relatively low temperatures and minimal time, and no strong acid or post-synthetic surface passivation was used.[44] So, the synthesis method is cost effective and green.

2.3. Synthesis of the Carbon Dot/Ag Heterostructure. The stock solution was made up of 0.1 g of $AgNO_3$ and 200 mL of deionized water (DI). A 3 mM solution of $AgNO_3$ was stirred for homogeneous mixing. Another stock solution was prepared by adding 0.009 g of $NaBH_4$ into 80 mL of DI accounting solution of the same strength (3 mM). Several CQD/Ag heterostructures were synthesized by mixing with a fixed amount of a previously synthesized CQD solution and different ratios of $AgNO_3$ and $NaBH_4$ at 120 °C for 2.5 h in a solvothermal oven. The synthesized CQD and CQD/Ag heterostructures were denoted as sample 1 (6 mL of CQD solution + 24 mL of DI), sample 2 (6 mL of CQD solution + 3 mL of $AgNO_3$ + 3 mL of $NaBH_4$ + 18 mL of DI), sample 3 (6 mL of CQD solution + 6 mL of $AgNO_3$ + 6 mL of $NaBH_4$ + 12 mL of DI), sample 4 (6 mL of CQD solution + 9 mL of $AgNO_3$ + 9 mL of $NaBH_4$ + 6 mL of DI), and sample 5 (6 mL of CQD solution + 12 mL of $AgNO_3$ + 12 mL of $NaBH_4$ + 0 mL of DI). $NaBH_4$ was used to reduce the $AgNO_3$. The obtained solution was washed three times with DI by ultracentrifugation at 20,000 rpm for 10 min. After preparing the samples, we stored it in a freezer at 4 °C for future experimentation.

https://doi.org/10.1021/acsomega.2c04964
ACS Omega 2023, 8, 4566−4577

2.4. Characterization. The synthesized particles were characterized by Fourier transform infrared spectroscopy (FTIR, IR Prestige, Shimadzu), ultraviolet-visible (UV−vis) spectroscopy (JASCO V650), and transmission electron microscopy (TEM, JEM2100, JEOL). The photoluminescence property was measured using Model FL3-11, Horiba JobinYvon, Fluorolog-3, Nanolog. Time-correlated single-photon counting (TCSPC) was done using the IBH fluorocube apparatus. Decay profiles were collected using a Hamamatsu MCP photomultiplier (R3809) with IBH DAS6 software. For TEM analysis, 5 mg of the sample was dispersed into absolute ethanol for 5 min under sonication; this was followed by the coating of the sample on a copper grid followed by drying in air before analysis. For FTIR and TCSPC, a powder sample was applied.

2.5. Cell Lines and Chemicals. Human colorectal carcinoma (HCT 116) and human embryonic kidney (HEK 293) cell lines were acquired from the National Centre for Cell Sciences (NCCS), Pune, India. Other essential components like penicillin−streptomycin−neomycin (PSN) antibiotic cocktail, Dulbecco's modified Eagle's medium (DMEM), ethylenediaminetetraacetic acid (EDTA), fetal bovine serum (FBS), and trypsin, required for cell culture media, were purchased from Gibco (Grand Island, NY). Other compulsory raw chemicals were procured from both Sigma-Aldrich, St. Louis, MO, and Sisco Research Laboratories (SRL), Mumbai, India, respectively. All necessary antibodies were collected from eBioscience, San Diego, and Santa Cruz Biotechnology, Dallas, Texas.

2.6. Cell Culture. Briefly, HCT 116, BJ-5ta, and HEK 293 cells were cultured at 37 °C in a humidified atmosphere under 5% CO_2 with DMEM (Dulbecco's modified Eagle' medium) containing 1% antibiotic (PSN) and 10% fetal bovine serum (FBS). After getting confluent (75−80%), cells were harvested with trypsin and EDTA in phosphate-buffered saline (PBS) and plated at the desired density to allow them to re-equilibrate before the experimentation.[45]

2.7. MTT Assay. The MTT assay was carried out to screen the cytotoxic effect of the synthesized sample.[46] The HCT 116 and HEK 293 cells were plated in a 96-well plate and treated with or without different concentrations of samples 1, 2, 3, 4, and 5 and incubated for 12 h at 37 °C in a humidified CO_2-rich condition (5%). After that, the cells were meticulously washed with PBS, followed by the addition of MTT solution (4 mg/mL), and incubated for another 4 h. After the incubation period of MTT, the absorbance of the acidic isopropanol-solubilized intracellular formazan salt was measured at 595 nm using an ELISA reader (Emax, Molecular Device). In all cases, the samples were sonicated before treating in the cell line to get homogenized mixtures.

2.8. Quantification of Apoptosis Using Flow Cytometry. Determination of apoptosis and necrosis was done by flow cytometry using an Annexin-V FITC/PI apoptosis/necrosis detection kit (Calbiochem, CA).[47] After treatment, the cells (1×10^6) were washed and stained with Annexin-V FITC and PI, followed by the manufacturer's instructions. The percentages of viable, apoptotic (early and late), and necrotic cells were evaluated by flow cytometry (BD LSRFortessa, San Jose, CA).

2.9. Live Cell Imaging for Cellular Uptake of Sample 5 in the HEK 293 Cell Line. HEK 293 cells were seeded at a density of 4×10^5 cells into a coverslip, dipped in the experimental medium, and incubated for 24 h before treatment. After discarding the medium, cells were treated with 6 μg/mL of sample 5 for 12 h duration, where Nuclear Red LCS1 was used as a nuclear stainer. After 12 h of treatment, the cells were washed and fixed on a slide. The fluorescence intensity of the stained cells was measured using a confocal laser-scanning microscope (FV 10i, Olympus, Japan).[48]

2.10. Estimation of Intracellular Reactive Oxygen Species (ROS). The generated intracellular reactive oxygen species (iROS) was measured using confocal microscopy with the help of an oxidation sensor dye, 2′,7′-dichlorofluorescein diacetate (H2DCFDA). The intensification of the green fluorescence intensity in confocal images was used to quantify the generation of iROS, where untreated cells were treated as control. The treated and untreated cells were plated on a coverslip. After the incubation time, fixation was completed. Then the cells were stained with H2DCFDA in the presence of Nuclear Red LCS1 and Mitotracker. The internalization of sample 5 was also visualized in a time-dependent manner. Stained cells were examined using a confocal laser-scanning microscope (FV 10i, Olympus, Japan).[49]

2.11. Caspase Activity Analysis. Caspase 3 activity was evaluated using the Caspase 3 activity assay kit, Biovision.[50] Precisely, cells were lysed in lysis buffer by 10 min incubation on an ice bucket. Cytosolic supernatants were isolated following centrifugation at 10,000*g* for 10 min. Hundred micrograms of protein diluted in 50 μL of cell lysis buffer was added. 4 mM DEVD-pNA was used as the substrate and incubated at 37 °C for 1−2 h. The absorbance was measured at 405 nm and the estimated data were reported as the amount of release of pN Umol/min/mg protein. Caspase 9 activity analysis was carried out by following the guideline of the kit protocol, Merck Millipore. Cells were isolated through Trypsin-EDTA treatment. After that, the cell suspension was washed with PBS and incubated with 1 μL of FITC-IETD-FMK at 37 °C for 0.5−1 h. Then, the cells were thoroughly washed and fluorescence intensity was determined using an LS55 spectrofluorometer (Perkin-Elmer) (Ex: 485 nm; Em: 535 nm).

2.12. Confocal Microscopical Analysis. HCT 116 cells were seeded on cover slips. After the seeding, the cells were incubated for 24 h. After the incubation time, 6 μg/mL sample 5 was taken to treat the HCT 116 cells. After the treatment, the cells were incubated for a proper time period. Untreated cells were taken as the control. Then, the control/treated cells were washed twice for 10 min each in PBS (0.01 M) and incubated for 1 h in a blocking solution containing 0.3% Triton X-100 and 2% normal bovine serum, in PBS. After blocking, the cells were incubated at 4 °C overnight with the respective primary antibody (BCL2, AKT, and cytochrome *c*), followed by washing and incubation with the respective fluorophore-conjugated secondary antibodies for 2 h. After that, the slides were counterstained with Nuclear Red LCS1 and mounted with the Prolong Anti-fade Reagent (Molecular Probe, Eugene, OR). Finally, the stained cells were scanned using a confocal laser-scanning microscope (FV 10i, Olympus, Japan).[51]

2.13. Statistical Analysis. Results were represented as the mean ± SEM of multiple data points. The statistical importance of the difference was calculated by analysis of variance (ANOVA) using OriginPro (version 8.0) software, where $p < 0.05$ was considered as significant.[33]

https://doi.org/10.1021/acsomega.2c04964
ACS Omega 2023, 8, 4566−4577

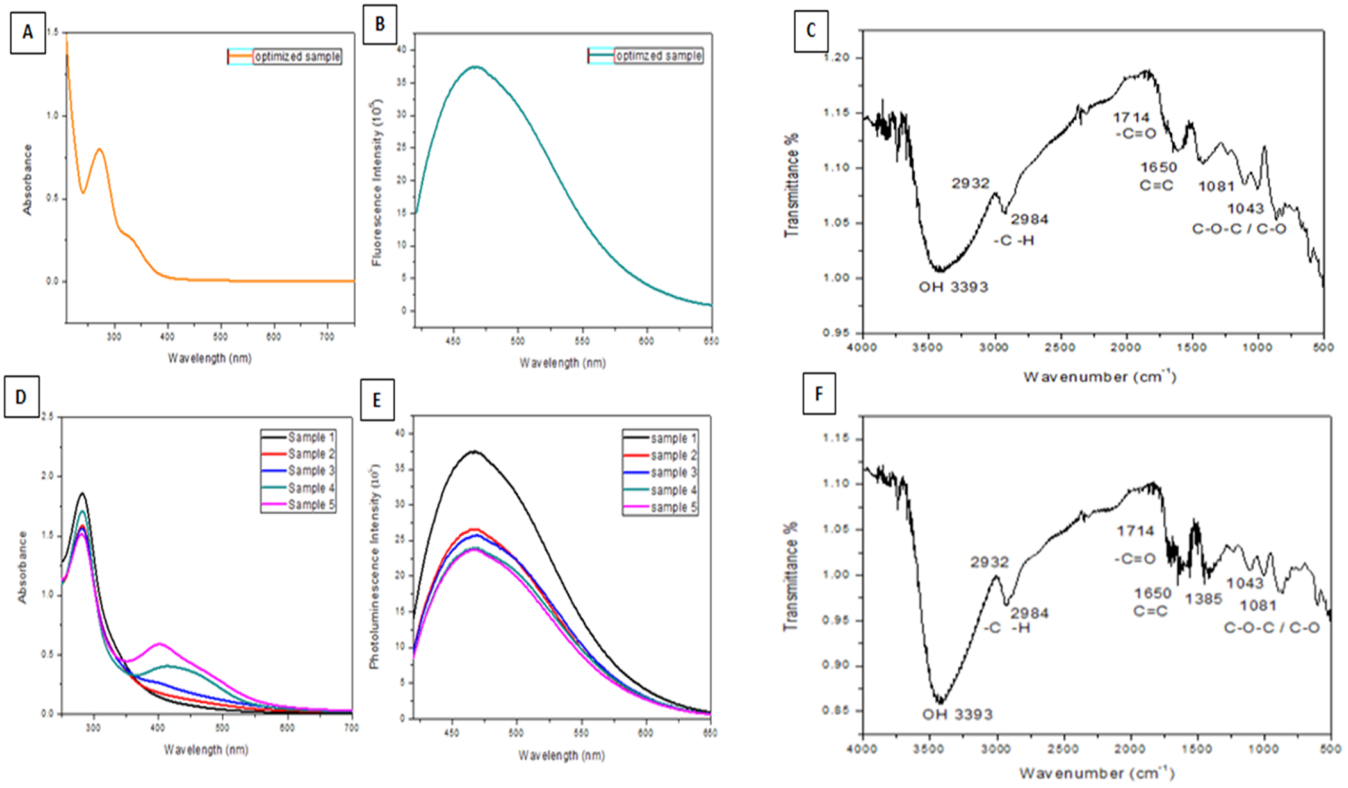

Figure 1. (A) UV−VIS, (B) photoluminescence, and (C) FTIR spectroscopy of carbon quantum dots; (D) UV−vis, (E) photoluminescence, and (F) FTIR spectroscopy of the carbon quantum dot silver heterostructure.

3. RESULTS AND DISCUSSION

3.1. UV−Visible Absorption and Photoluminescence Property. The UV−visible absorption has been presented in Figure 1A. CQDs showed a broad UV absorption peak at 271 nm, which is consistent with the carbon nanoparticles synthesized by carbonization. The photoluminescence spectra (Figure 1B) of CQDs reflected a prominent emission peak at 467 nm with an excitation wavelength of 415.8 nm. The optical properties of the CQDs vary with size, which could also result in the variation in density and nature of sp2 sites available in the CQDs. This was also demonstrated in a repetition of the experiment. Meanwhile, the broad UV−vis absorption spectrum of CQD/Ag heterostructures with an SPR peak at 460 nm (Figure 1D) was attributed to the ensemble light absorption resulting from the clustering effect of the silver nanoparticles on the carbon dot. The data displayed a surface plasmon resonance peak at 450 nm, which is consistent with the results obtained by Hyosung Choi et al.[52] Systematic variation of the UV−Vis spectroscopy data was observed from the synthesized samples (Figure 1D). From the figure, it is found that the SPR peak was at around 450 nm for all of the samples, which confirmed the proposed CQD/Ag heterostructure formation. Figure 1E displays the PL spectra of the CQD/Ag heterostructure at an excitation wavelength of 415.8 nm. The intensity of the greenish-blue emission decreased for the CQD/Ag heterostructure with no change in peak position. This accounts for the interaction between the exciton of CQDs and surface plasmons of Ag nanoparticles. The recombination rate of electrons and holes decreased, which resulted in low PL intensity. The Ag nanoparticles attached over CQDs act as traps for the photogenerated electrons and quench the PL emission. As the CQDs and Ag nanoparticles are in direct contact, electron transfer takes place between the energy levels of CQDs and Ag.

3.2. FTIR Spectroscopy. The FTIR spectrum (Figure 1C) was recorded to investigate the bonding composition of the carbon dot and its functional groups. CQDs exhibited a sharp peak centered at 1650 cm^{-1} assigned to the aromatic C═C stretching vibration, which is the elementary unit of the CQDs. In addition, CQDs showed a broad band in between 3300 and 3500 cm^{-1} due to the O−H stretching vibration and three sharp peaks at 1708, 1081, and 1043 cm^{-1} assigned to C═O, C−O−-C, and C−O stretching vibrations, which confirmed the existence of carboxylate and hydroxyl groups on the surfaces. The presence of these functional groups impart excellent solubility in water without further chemical modification. Furthermore, these functional groups can be modified for potential applications in drug delivery, biosensing, and biomedical imaging. In the case of the CQD/Ag heterostructure (Figure 1F), a sharp peak centered at 1650 cm^{-1} was also obtained. The appearance of a broad peak centered at 3300−3500 cm^{-1} (O−H vibrational stretch), a sharp peak at 1708 cm^{-1} (C═O vibrational stretch), and peaks at 1081 and 1043 cm^{-1} (C−O−C/C−O vibrational stretch) suggested the existence of carboxylate and hydroxyl groups on the surfaces. Moreover, the CQD/Ag heterostructure displayed an additional prominent peak at 1385 cm^{-1}, ascribed to the presence of silver nanoparticles, and the result is consistent with Devaraj et al.[53]

3.3. FESEM-EDX and TEM Analysis. To further confirm the different ratios of Ag in several CQD/Ag heterostructures, we carried out field emission scanning electron microscopy-energy-dispersive X-ray (FESEM-EDX) elemental mapping along with EDX spectra analysis. As shown in Figure 2 (A,B),

https://doi.org/10.1021/acsomega.2c04964
ACS Omega 2023, 8, 4566−4577

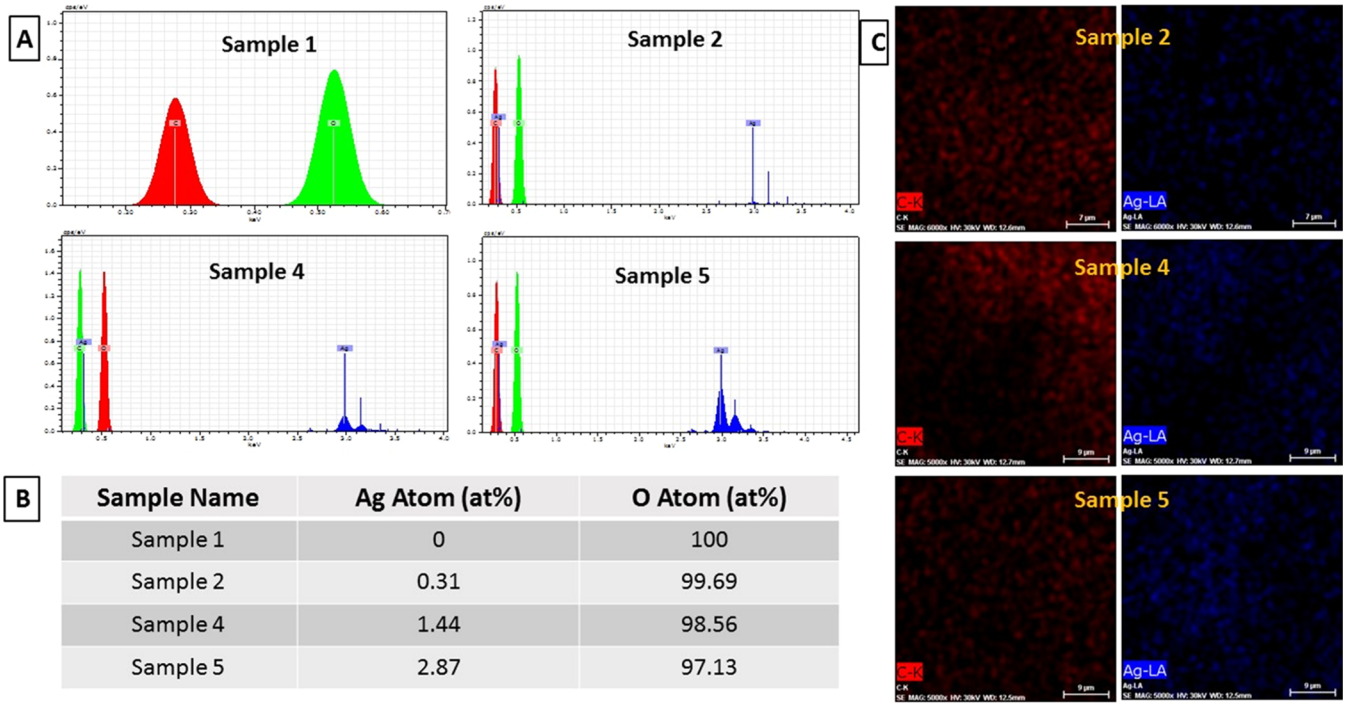

B

Sample Name	Ag Atom (at%)	O Atom (at%)
Sample 1	0	100
Sample 2	0.31	99.69
Sample 4	1.44	98.56
Sample 5	2.87	97.13

Figure 2. (A) FESEM-EDX spectra and (B) elemental atomic percentage of samples 1, 2, 4, and 5. (C) Elemental mapping images of samples 2, 4, and 5.

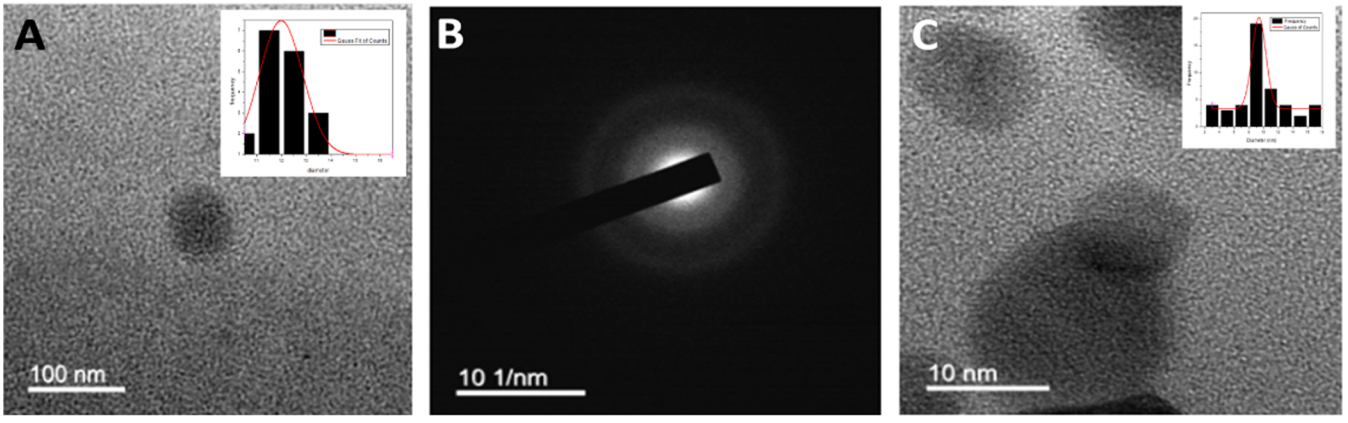

Figure 3. (A) TEM images of the carbon quantum dots (particle size distribution plot is in the inset); (B) SAED pattern of the carbon quantum dots; (C) TEM image of the carbon quantum dot silver heterostructure (particle size distribution plot is in the inset).

representative EDX spectra of the synthesized samples 1, 2, 4, and 5 undoubtedly confirmed the enhancement in the atomic percentage of Ag atom gradually. Here the "O" atom assigned to the surface-adsorbed oxygen arose from the experimental sample preparation condition. Moreover, the elemental mapping analysis (shown in Figure 2(C)) of representative samples 2, 4, and 5 clearly revealed that C and Ag were uniformly distributed in the heterostructures. Additionally, it had been observed that the intensity of the Ag atom in the images gradually increases with increasing Ag concentration, which further confirmed the enhancement of Ag from sample 2 to sample 5. No other elements were observed in the results of elemental analysis; hence, it proves that the sample was prepared in pure.

Meanwhile, in the morphological investigation as shown in Figure 3A, the TEM images of CQDs prepared from the orange juice extract reveal that they had uniform dispersion without apparent aggregation and all of them are spherical in shape. The size distribution histogram was obtained by counting 200 particles and the average diameter was estimated to be around 12 nm by Gaussian fitting (as shown in the inset). The high-resolution TEM (HRTEM) images of single particles are amorphous in nature. The SAED pattern in Figure 3B displayed rings indicating the amorphous nature of the synthesized carbon dots. The TEM samples were prepared by drop casting a diluted solution of the CQD/Ag heterostructure onto a carbon-coated copper grid and dried under vacuum before the analysis. The size distribution of silver was statistically evaluated using Image J software. In Figure 3C, the TEM images of the CQD/Ag heterostructure prepared from the orange juice extract reveal that they have uniform dispersion without apparent aggregation and all of them are spherical in shape. The size distribution histogram was obtained by counting 60 particles and the average

https://doi.org/10.1021/acsomega.2c04964
ACS Omega 2023, 8, 4566−4577

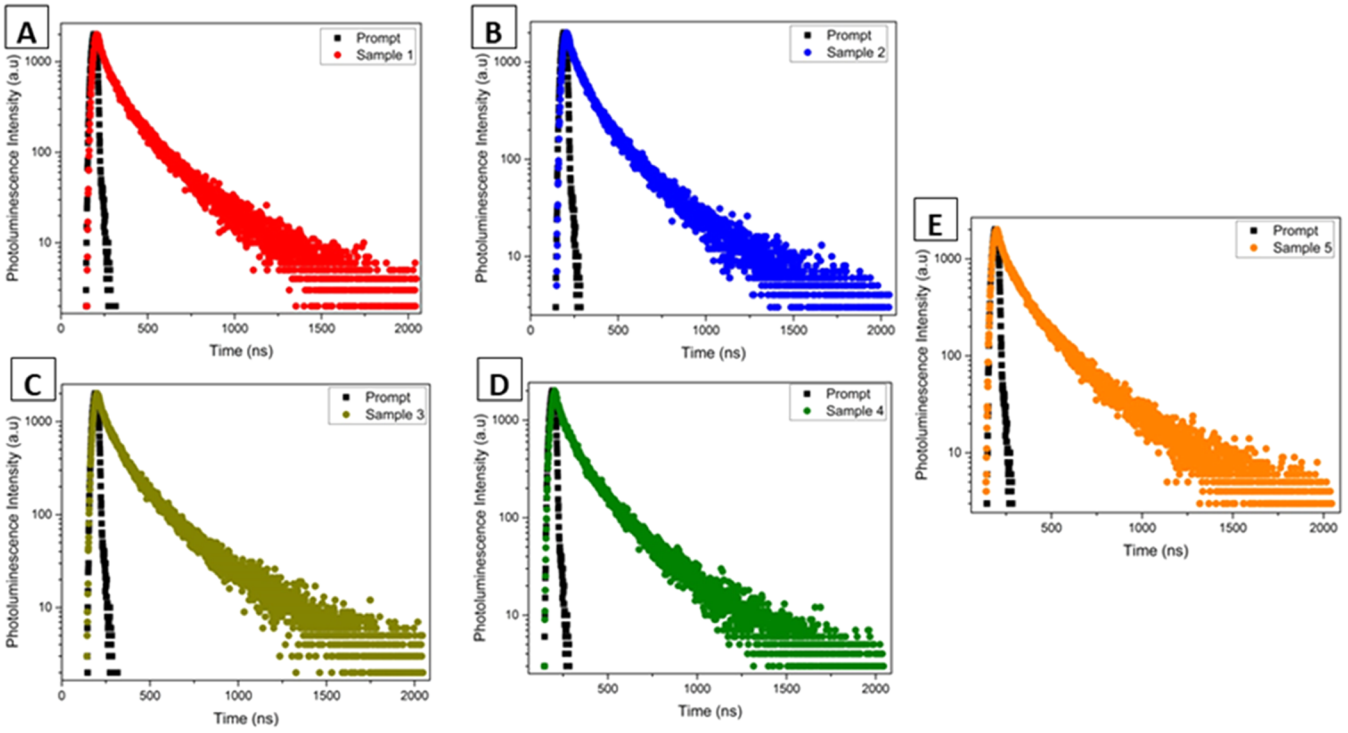

Figure 4. (A–E) TCSPC data of 5 Samples.

diameter was estimated to be around 10 nm by Gaussian fitting (as displayed in the inset). The high-resolution TEM (HRTEM) images of a single particle of CQD/Ag were crystalline in nature.

3.4. Photoluminescence Decay Profile of the CQD/Ag Heterostructure. The photoluminescence decay profiles observed for samples 1, 2, 3, 4, and 5 are presented in Figure 4(A–E). From the decay values, the photoluminescence decay time (exciton lifetime) was calculated to be 2.24, 2.17, 2.08, 1.99, and 1.96 ns, respectively, for samples 1, 2, 3, 4, and 5. This data is presented in Table 2 under T1 value, which accounts for radiative transitions. The nonradiative transition lifetime is also tabulated in this table under T2 column. 8.96, 8.69, 8.34, 7.96, and 7.86 ns are the corresponding lifetimes associated with samples 1, 2, 3, 4, and 5, respectively. The data from Table 2 suggested that the lifetimes of radiative transitions and lifetimes of nonradiative transitions are both reduced subsequently, which indicates the electron transfer between the carbon dots and silver nanoparticles. The basic theory of photoluminescence explains the reduced number of lifetime carbon dots due to the recombination of excited electrons in the conduction band with holes in the valence band through the additional path provided by the silver nanoparticle.

Table 2. TCSPC Table for T1 and T2. T1 Accounts for Radiative Transitions and T2 Accounts for Nonradiative Transitions

		time period at wavelength (in ns)	
sl. no.	sample	478 nm	
		T1	T2
1.	sample 1	2.24	8.96
2.	sample 2	2.17	8.69
3.	sample 3	2.08	8.34
4.	sample 4	1.99	7.96
5.	sample 5	1.96	7.86

3.5. Photostability Study. In aqueous solution, the CQD/Ag and CQD heterostructure displayed notable photostability. The absorbance plots of all of the samples in Figure 5 A–E showed that the absorbance center wavelength and the absorbance peak remained unaffected, whereas the absorbance intensity reduced to less than 40% after 4 h of exposure compared to the native intensity. Additional factors influencing the absorbance of samples are pH and ionic strength of the solvent, leading to changes in the surface status of the CQDs.[54] It is also expected that degrading absorbance is a consequence of changes in the structure of functional groups at the surface. The extent of degradation is mostly dependent on the intensity of exposure to light and duration, but it also depends on the CQDs' concentration. The lower the concentration, the easier the fluorescence bleaching of CQDs. The extent is calculated in our experiment is by the formula

$$\%\ \text{of degradation} = \frac{\text{absorbance}(0\ \text{h UV}) - \text{absorbance}(\ x\ \text{h UV})}{\text{absorbance at}\ \ 0\ \text{h uv exp osure}} \times 100$$

By this formula we can define quantitatively the extent of degradation in the samples under ultraviolet light exposure for a prolonged time. Table 3 shows the different absorbance values of the samples with different times of UV exposure. The synthesized samples show excellent photostability, degraded up to a maximum of 37 and a minimum of 29%, which is very promising for use as a cellular imaging agent.

3.6. Estimation of Effective Remedial Dose of CQD/Ag against Colon Cancer Cells. The external surface of the CQDs contains functional groups, which can act as nucleation sites for attachment of metallic NPs like Ag or Au. A recent

https://doi.org/10.1021/acsomega.2c04964
ACS Omega 2023, 8, 4566–4577

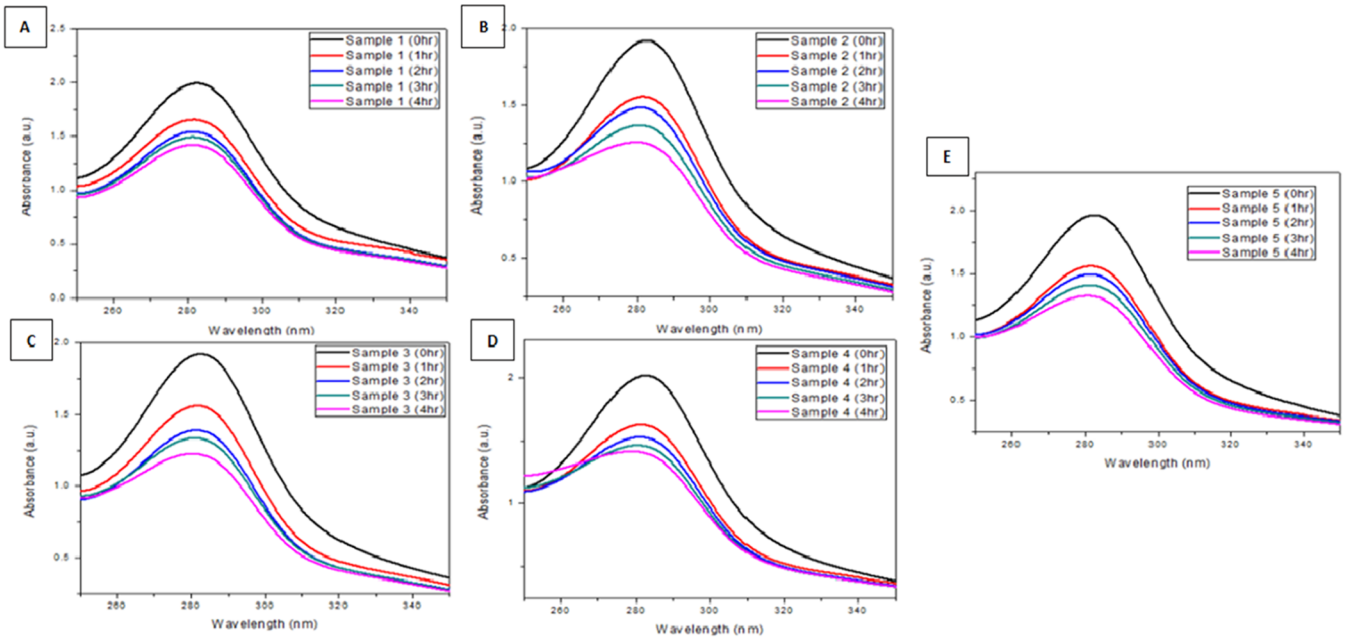

Figure 5. (A–E) Absorbance of sample 1 to sample 5 after irradiation for 1, 2, 3, and 4 h in ultraviolet light.

Table 3. Degradation % of Samples (1, 2, 3, 4, 5) Under UV Irradiation for 1, 2, 3, and 4 h

sl. no.	sample	0 h (%)	1 h (%)	2 h (%)	3 h (%)	4 h (%)
1.	sample 1	0	17	23	25	29
2.	sample 2	0	19	23	28	35
3.	sample 3	0	19	28	31	37
4.	sample 4	0	19	24	28	31
5.	sample 5	0	20	24.5	28	33

analysis by Liu et al. suggested that heterostructures/hybrid metallic CQDs have more remedial as well as theranostics efficacy than the uni-structure of either metallic NPs or CQDs.[56] According to reports, the extract of orange contains a high content of berberine, an alkaloid with a high therapeutic application. According to Wang et al., berberine, a small isoquinoline alkaloid, shows its therapeutic efficacy on diarrhea, and bacterial and fungal diseases.[55] Recent studies have also suggested that berberine attenuates cancer cell proliferation by restricting the cell cycle and inducing the apoptotic process.[39] Researchers have also demonstrated that berberine can induce autophagy and also stops the invasion process as well as metastasis in various types of cancer.[56]

So, by analyzing the efficacy of CQD/Ag, an optimum therapeutic dose was evaluated through the *in vitro* way. HCT 116 cells were considered as an *in vitro* primary malignant epithelial colon carcinoma model, as they functionally replicate a similar physiology as that of primary aggressive human colon cancer.[57] MTT analysis suggested that administration of 6, 8, 10, 12, 14, 16, 18, and 20 μg/mL concentrations of samples 1–5 for 24 h can induce more than 50% of cell death, while samples 1, 2, 3, and 4 displayed similar effects at notably higher concentrations of 20, 18, 14, and 12 μg/mL, respectively ($p < 0.01$). Hence, administration of a lower concentration of

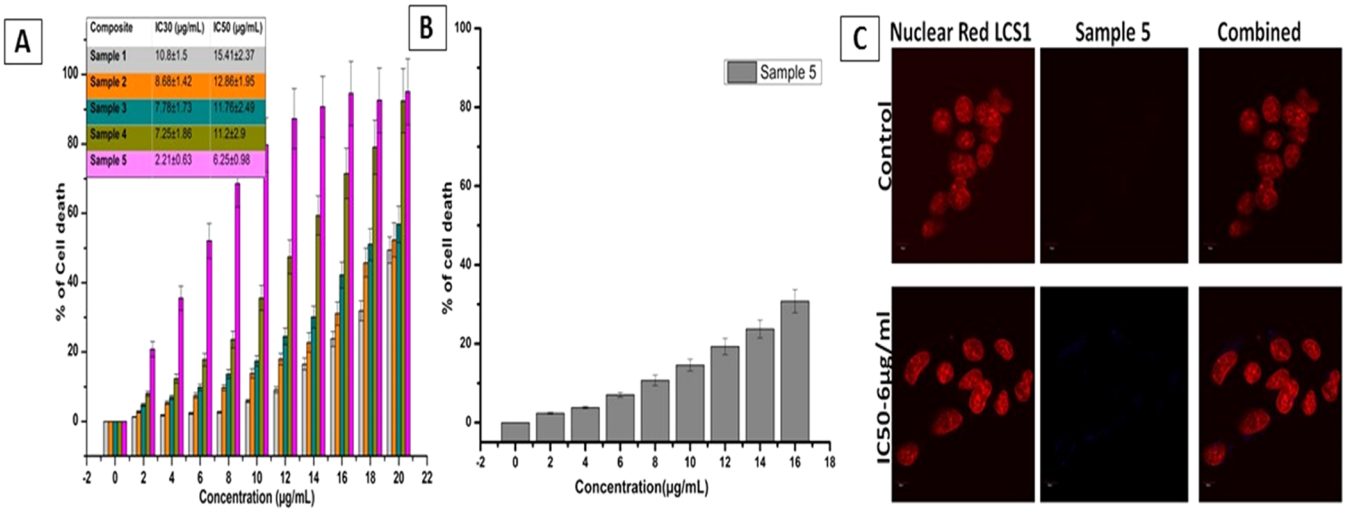

Figure 6. (A) MTT assay data (samples 1-5) against the HCT 116 cell line (IC50 values have been incorporated in the inset). (B) MTT assay of sample 5 against the BJ-5ta cell line. (C) Cellular penetration of sample 5 in HEK 293.

https://doi.org/10.1021/acsomega.2c04964
ACS Omega 2023, 8, 4566–4577

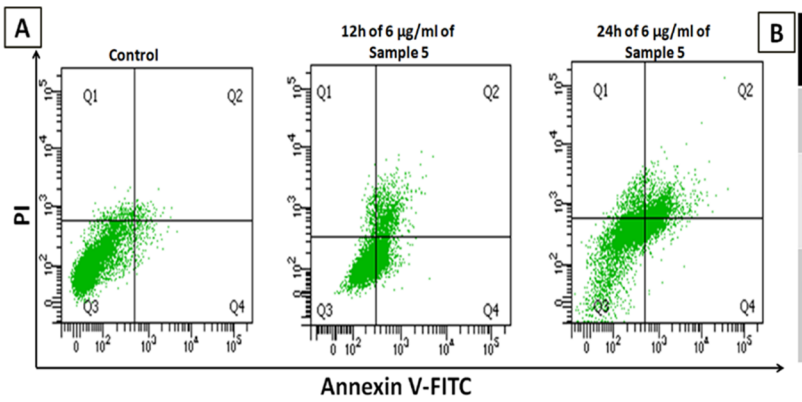

B

	Q1(Necrosis)	Q2 (Late Apoptosis)	Q3 (Live cell)	Q4(Early Apoptosis)
Control	2.8%	1.6%	92.9%	2.7%
12h of 6 µg/ml of Sample 5	2.2%	9.5%	73.5%	14.8%
24h of 6 µg/ml of Sample 5	7.1%	22.8%	46.3%	23.8%

Figure 7. (A) Annexin-V FITC assay data after treatment of 6 μg/mL of sample 5 against the HCT 116 cell line (time-dependent study) (incorporated in the inset). (B) Quantification of cells in each quadrant of the FACS data.

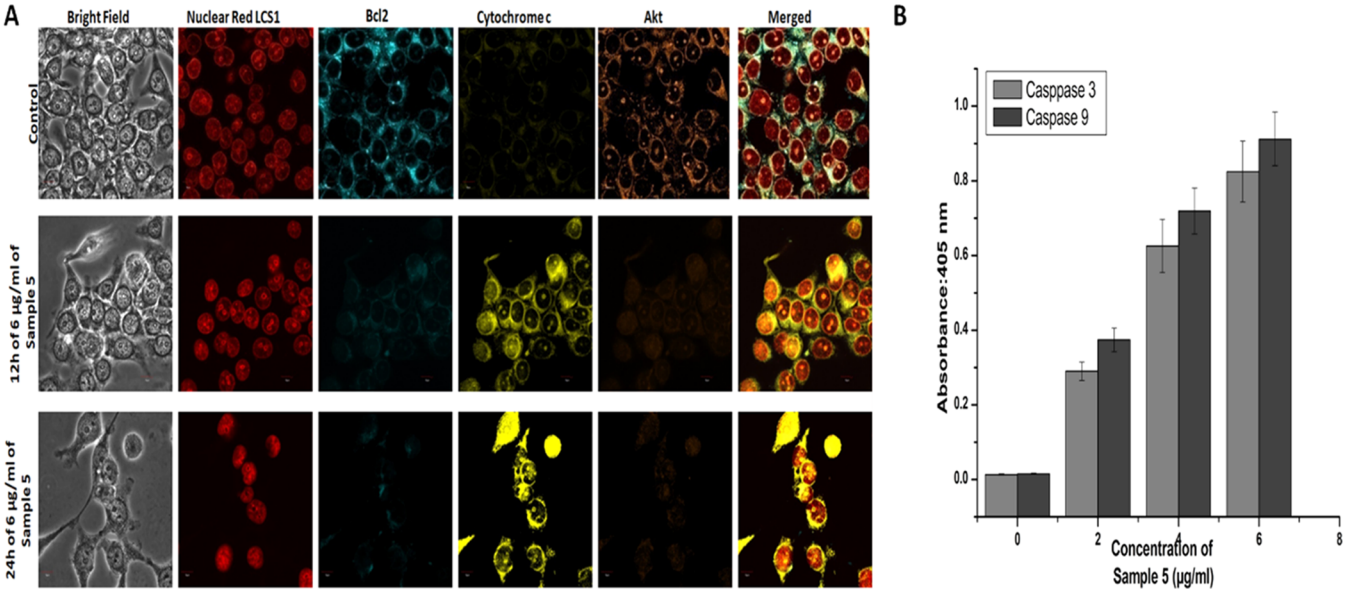

Figure 8. (A) Measurement of Bcl2, AKT, and cytochrome *c* intensity of sample 5 (time-dependent study) in the presence of Nuclear Red LCS1. (B) Caspase 3 & 9 activity after dose-dependent treatment of the sample.

sample 5 (0, 2, and 4 μg/mL) was not able to induce a significant amount of cell death within a 24 h experimental tenure. Considering the findings, 6 μg/mL of sample 5 was considered as the lowest effective dose that can induce a significant amount [>60%] ($p < 0.01$) of cell death in HCT 116 cells and was selected for further experimental validations (Figure 6A). The biocompatibility of sample 5 was also checked in the BJ-5ta cell line (Figure 6B), which showed that up to 12 μg/mL sample 5 is biocompatible, but above 12 μg/mL the heterostructure exhibits cell death. A similar analysis with noncancerous HEK 293 cells evidently demonstrated that 6 μg/mL of sample 4 administration induces a very negligible [>10%] ($p < 0.01$) amount of cell death (Figure 6C). Therefore, treatment with sample 5 at 6 μg/mL may be recommended as nonhazardous for healthy noncancerous cells.

3.7. Exploration of Cell Death at the Lowest Effective Dose of Sample 5 in Colon Cancer Cells. Reduction of a significant amount of cell survivability after sample 5 administration led us to analyze the actual reason behind this alteration in HCT 116 cells. The data pointed toward apoptotic incidence. Annexin-V/PI staining followed by flow-cytometric study demonstrated 24.3% (14.8% early apoptotic and 9.5% late apoptotic) cells after 12 h of drug administration, whereas only 2.2% of the cell population were in the necrotic quadrate. Surprisingly, a percentage of the apoptotic cells were significantly increased to 46.4% (22.8% early apoptosis and 23.6% late apoptosis) after 24 h of 6 μg/mL sample 5 treatment (Figure 7. A, B) as compared with other treated or untreated sets. On the basis of the above-mentioned values, 24 h of sample 5 treatment was considered to specifically induce apoptosis, the prime reason for suppression of HCT 116 cell survivability, as evaluated by analyzing the externalization of phosphatidylserine. The data also demonstrated that a majority of the cell population was shifted toward the early apoptotic quadrate as compared with untreated HCT 116 cells. This indicated the efficacy of sample 5.

3.8. Evaluation of the Status of Apoptosis-Modulatory Caspases after Sample 5 Administration. According to many researchers, caspases play a cardinal role in the apoptosis procedure.[58] Expansion of the cell population in both apoptotic quadrates evidently portrayed an elevated level of caspase activity. Caspase 3, which is an executioner caspase, can be activated by the initiator caspase, Caspase 9-appropriate intrinsic cues.[59] The data clearly showed significant augmenta-

https://doi.org/10.1021/acsomega.2c04964
ACS Omega 2023, 8, 4566−4577

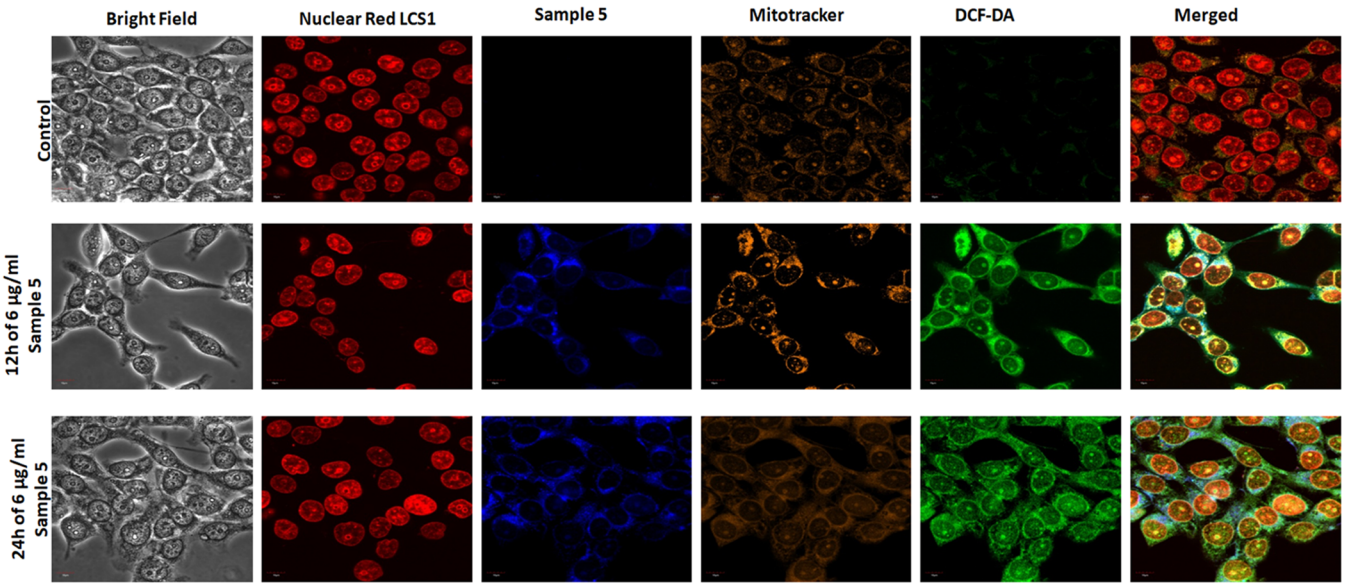

Figure 9. Measurement of DCF-DA and the fluorescence intensity of sample 5 (time-dependent study) in the presence of Nuclear Red LCS1 and Mitotracker.

tion in caspase 3 and caspase 9 activity after drug exposure in HCT 116 cells ($p < 0.01$). The results further portrayed a gradual increase in both caspases' activity with increasing drug concentration. This notable observation points out a distinct positive correlation between the rate of apoptosis and both caspases' activity (Figure 8B).

3.9. Elevation in the Pro-apoptotic Regulatory Cytochrome *c* Triggers the Apoptotis Procedure in HCT 116 cells after Sample 5 Treatment. Increase in the caspase 9 level is mainly controlled by various apoptotic pathways.[60] The cytochrome *c*−caspase 9 axis plays a guardian role in programmed cell death by inducing factors of the intrinsic apoptotic pathway.[61] Activated by intrinsic cues like elevated reactive oxygen species (ROS) level, cytochrome *c* is released from the mitochondria to cytoplasm and induces apoptotic process by targeting initiator caspases.[62] Confocal microscopical analysis portrayed a significant increase in cytochrome *c* level and its cytoplasmic localization after 12 h of sample 5 treatment, while the increase was extremely high after 24 h of treatment schedule. This result positively supports previous findings. However, no significant alteration was noticed in the 15 μg/mL sample 5-treated group. Localization of cytochrome *c* in the cytoplasm is also modulated by the Bcl2 group of proteins.[63] Bcl2 restricts the mitochondrial localization of cytochrome *c* and attenuates apoptosis (Figure 8A). In the present study, the data depicted a significant amount of reduction in Bcl2 level in the treated groups in comparison with untreated HCT 116 cells ($p < 0.05$). Clinical studies have shown overexpression of Akt in various types of cancer, especially in colorectal cancer.[64] Akt is a serine/threonine kinase that critically modulates the growth factors and increases the rate of cell survivability by stabilizing the inhibitory Bcl2 protein followed by attenuation of the apoptotic process, which in turn makes the cancer cells technically immortal in nature.[65] In the current analysis, the data clearly showed a significant amount of reduction of the Akt level in the treated group of cells, especially in the 12 and 24 h sample 5-administered groups. It was notable that the level of reduction was highest in the 24 h sample 5-administered cells as compared with the other two treated groups (Figure 8A).

Therefore, it may be said that our drug induced apoptosis in the colon cancer cell line by attenuating the Akt-BCL2 axis and also turned on the Cytochrome *c*-mediated intrinsic apoptosis pathway. Colon cancer is a very common cancer with a high mortality rate. Several studies show augmented expression of antiapoptotic proteins like Akt, PKC, and Bcl2 in colorectal cancer tumors.[66] In our study, the results depicted that administration of our drug suppresses cell survivability in a significant manner. ROS-mediated DNA damage induces p53 phosphorylation, which in turn stabilizes p53, indispensable to counter tumorigenic growth and differentiation.[67] Cell death is a sequential process; increase in stabilized p53 attenuates the antiapoptotic Bcl2 group of proteins and also restricts cell survival modulatory proteins like Akt.[68] Studies have also noted that increase in stabilized p53 increases the expression of the pro-apoptotic Bax protein,[69] which destabilizes the mitochondrial membrane potential and makes it porous in nature, which in turn augments release of the apoptotic inducer cytochrome *C* proteins in the cytoplasm.[70] In the present study, confocal microscopic analysis evidently pointed out a significant amount of increase in the cytoplasmic cytochrome *C* concentration and attenuation of cell survival modulatory Akt and Bcl2 groups of proteins. This was clearly supported by the decreasing values of cell survivability analysis after sample 5 treatment. The results also clearly suggested that the restriction of HCT 116 survivability by sample 5 was due to the turning on of apoptotic pathways, which was not seen in the control cell lines.

Apoptotic body formation in the cell lines was noticed by analyzing the Annexin-V FITC-stained cell population, which was gradually increased with drug concentration. Caspase 3 and 9 activities were also noticed in our treated groups. Accumulation of sample 5-mediated mitochondrial ROS played a key therapeutic as well as theranostic role that not only induced apoptosis but also illuminated the fluorescence after entry into HCT 116 cells. Surprisingly, our results also showed an unaltered control cell population and did not show

https://doi.org/10.1021/acsomega.2c04964
ACS Omega 2023, 8, 4566−4577

any significant effect on the HEK 293 cell line. The increased cytochrome *c* expression along with its cytoplasmic localization in a dose-dependent manner indicated drug-induced modulation in pro- and antiapoptotic modulatory proteins as well as its causative inducing mechanism. Several studies have pointed out that release of cytochrome *c* in the cytosol requires an ROS-mediated destabilized mitochondrial membrane.[71−74] Surprisingly, our study showed a notably increased amount of mitochondrial ROS, which was visualized as elevated DCF-DA fluorescence (Figure 9), and its colocalization with Mitotracker Orange, a fluorescence marker specialized for denoting mitochondria, and sample 5 indicated a significant level of mitochondrial penetrance of the said CQD (Figure 9) as compared with the control HEK 293 cells (Figure 6C).

Therefore, our drug after entering into mitochondria destabilized its membrane. Release of Cytochrome *c* in the cytosolic region results in induced apoptosis in HCT 116 cells. The results also indicated the crucial role of mitochondrial ROS after sample 5 treatment, which may be the possible cue for destabilization of the mitochondrial membrane resulting in turning on the Cytochrome *c*−Caspase 9−Caspase 3 intrinsic apoptotic axis.

4. CONCLUSIONS

In conclusion, we have demonstrated a facile, green synthesis method of CQDs from a cheap and readily available natural precursor. After that, CQD/Ag heterostructures were synthesized using different ratios of $AgNO_3$. These partially crystalline carbon nanoparticles show strong and stable photoluminescence. The CQD/Ag heterostructure does not show any cytotoxicity to healthy cells and is efficiently taken up by the cells. Moreover, the flow-cytometric data and confocal microscopic images confirmed that the heterostructure showed a strong anticancer potential at 6 μg/mL via the ROS-dependent mitochondrial-mediated apoptosis pathway, where Akt plays an important role. In addition, the heterostructure has bioimaging ability.

AUTHOR INFORMATION

Corresponding Author

Chandan Kumar Ghosh − *School of Material Science and Nanotechnology, Jadavpur University, Kolkata 700032, India;* orcid.org/0000-0002-6086-2249; Email: chandu_ju@yahoo.co.in

Authors

Snehasis Mishra − *School of Material Science and Nanotechnology, Jadavpur University, Kolkata 700032, India*

Kaustav das − *School of Material Science and Nanotechnology, Jadavpur University, Kolkata 700032, India*

Sujan Chatterjee − *Molecular Biology and Tissue Culture Laboratory, Post Graduate Department of Zoology, Vidyasagar College, Kolkata 700006, India*

Panchanan Sahoo − *School of Material Science and Nanotechnology, Jadavpur University, Kolkata 700032, India;* orcid.org/0000-0003-2379-5822

Sudip Kundu − *School of Material Science and Nanotechnology, Jadavpur University, Kolkata 700032, India*

Mrinal Pal − *CSIR-Central Glass & Ceramic Research Institute, Council of Scientific & Industrial Research, Kolkata 700032, India;* orcid.org/0000-0002-1032-272X

Asim Bhaumik − *School of Materials Sciences, Indian Association for the Cultivation of Science, Kolkata 700032, India;* orcid.org/0000-0002-4907-7418

Complete contact information is available at: https://pubs.acs.org/10.1021/acsomega.2c04964

Author Contributions

The manuscript was written through contributions of all authors. All authors have given approval to the final version of the manuscript.

Notes

The authors declare no competing financial interest.

ACKNOWLEDGMENTS

The Junior Research fellowship and Inspire fellowship from CSIR, DST Govt. of India, awarded to S.K. and P.S., respectively, are gratefully acknowledged. The funding agency had no role in the design of the study; in the collection, analyses, or interpretation of data; and in the writing of the manuscript.

REFERENCES

(1) Haggar, F. A.; Boushey, R. P. Colorectal cancer epidemiology: incidence, mortality, survival, and risk factors. *Clin. Colon Rectal Surg.* **2009**, *22*, 191−197.

(2) Zhang, S.; Guo, S.; Li, Z.; Li, D.; Zhan, Q. High expression of HSP90 is associated with poor prognosis in patients with colorectal cancer. *Peer J.* **2019**, *7*, No. e7946.

(3) Dela Cruz, C. S.; Tanoue, L. T.; Matthay, R. A. Lung cancer: epidemiology, etiology, and prevention. *Clin. Chest Med.* **2011**, *32*, 605−644.

(4) Budreviciute, A.; Damiati, S.; Sabir, D. K.; Onder, K.; Schuller-Goetzburg, P.; Plakys, G.; Katileviciute, A.; Khoja, S.; Kodzius, R. Management and Prevention Strategies for Non-communicable Diseases (NCDs) and Their Risk Factors. *Front. Public Health* **2020**, *8*, No. 574111.

(5) Dekker, E.; Tanis, P. J.; Vleugels, J. L.; Kasi, P. M.; Wallace, M. B. Risk factors. *Lancet* **2019**, *394*, 1467−1480.

(6) Anand, A.; Unnikrishnan, B.; Mao, J. Y.; Lin, C. J.; Lai, J. Y.; Huang, C. C. Carbon-based low-pressure filtration membrane for the dynamic disruption of bacteria from contaminated water. *Water Res.* **2022**, *212*, 118121−118129.

(7) Lin, H. Y.; Wang, S. W.; Mao, J. Y.; Chang, H. T.; Harroun, S. G.; Lin, H. J.; Huang, C. C.; Lai, J. Y. Carbonized nanogels for simultaneous antibacterial and antioxidant treatment of bacterial keratitis. *Chem. Eng. J.* **2021**, *411*, No. 128469.

(8) Cha, C.; Shin, S. R.; Annabi, N.; Dokmeci, M. R.; Khademhosseini, A. Carbon-based nanomaterials: multifunctional materials for biomedical engineering. *ACS Nano* **2013**, *7*, 2891−2897.

(9) Bakry, R.; Vallant, R. M.; Najam-ul-Haq, M.; Rainer, M.; Szabo, Z.; Huck, C. W.; Bonn, G. K. Medicinal applications of fullerenes. *Int. J. Nanomed.* **2007**, *2*, 639−649.

(10) Shen, H.; Zhang, L.; Liu, M.; Zhang, Z. Biomedical applications of graphene. *Theranostics* **2012**, *2*, 283−294.

(11) Alshehri, R.; Ilyas, A. M.; Hasan, A.; Arnaout, A.; Ahmed, F.; Memic, A. Carbon nanotubes in biomedical applications: factors, mechanisms, and remedies of toxicity: miniperspective. *J. Med. Chem.* **2016**, *59*, 8149−8167.

(12) Chung, C.; Kim, Y. K.; Shin, D.; Ryoo, S. R.; Hong, B. H.; Min, D. H. Biomedical applications of graphene and graphene oxide. *Acc. Chem. Res.* **2013**, *46*, 2211−2224.

(13) Su, W.; Wu, H.; Xu, H.; Zhang, Y.; Li, Y.; Li, X.; Fan, L. Carbon dots: a booming material for biomedical applications. *Mater. Chem. Front.* **2020**, *4*, 821−836.

(14) Roy, R. K.; Lee, K. R. Biomedical applications of diamond-like carbon coatings: A review. *J. Biomed. Mater. Res., Part B* **2007**, *83B*, 72−84.
(15) Hu, Y.; Ji, W.; Sun, J.; Liu, X.; Zhou, R.; Yan, J.; Zhang, N. Simple and eco-friendly synthesis of crude orange-peel-derived carbon nanoparticles for detection of Fe3+ and ascorbic acid. *Luminescence* **2021**, *36*, 1385−1394.
(16) Wang, M.; Shi, R.; Gao, M.; et al. Sensitivity fluorescent switching sensor for Cr (VI) and ascorbic acid detection based on orange peels-derived carbon dots modified with EDTA. *Food Chem.* **2020**, *318*, No. 126506.
(17) Jian, H. J.; Yu, J.; Li, Y. J.; Unnikrishnan, B.; Huang, Y. F.; Luo, L. J.; Ma, D.H.K.; Harroun, S. G.; Chang, H. T.; Lin, H. J.; Lai, J. Y. Highly adhesive carbon quantum dots from biogenic amines for prevention of biofilm formation. *Chem. Eng. J.* **2020**, *386*, 123913−123925.
(18) Penniston, K. L.; Nakada, S. Y.; Holmes, R. P.; Assismos, D. G. Commercial Merchandising Custom Wooden Wine Storage Rack for Shop. *J. Endourol./Endourol. Soc.* **2008**, *22*, 567.
(19) Cruz, D. M.; Tian-Street, w.; Zhang, B.; Huang, X.; Crua A, V.; Nitro-Argüello, A.; Cholula-Díaz, J. L.; Martínez, L.; Huttel, Y.; González, M. U.; García-Martín, J. M.; Webster, T. J. Citric juice-mediated synthesis of tellurium nanoparticles with antimicrobial and anticancer properties. *Green Chem.* **2019**, *21*, 1982−1998.
(20) Pandey, K. B.; Rizvi, S. I. Plant polyphenols as dietary antioxidants in human health and disease. *Oxid. Med. Cell. Longevity* **2009**, *2*, 270−278.
(21) Nguyen, D. D.; Lai, J. Y. Synthesis, bioactive properties, and biomedical applications of intrinsically therapeutic nanoparticles for disease treatment. *Chem. Eng. J.* **2022**, *435*, 134970−134996.
(22) Abbasi, B. H.; Khan, T.; Khurshid, R.; Nadeem, M.; Drouet, S.; Hano, C. UV-C mediated accumulation of pharmacologically significant phytochemicals under light regimes in in vitro culture of Fagonia indica (L.). *Sci. Rep.* **2021**, *11*, No. 679.
(23) Molaei, M. J. Carbon quantum dots and their biomedical and therapeutic applications: a review. *RSC Adv.* **2019**, *9*, 6460−6481.
(24) Gomathi, A. C.; Rajarathinam, S.R.X.; Sadiq, A. M.; Rajeshkumar, S. Anticancer activity of silver nanoparticles synthesized using aqueous fruit shell extract of Tamarindus indica on MCF-7 human breast cancer cell line. *J. Drug Delivery Sci. Technol.* **2020**, *55*, No. 101376.
(25) Pardo, J.; Peng, Z.; Leblanc, R. M. Cancer targeting and drug delivery using carbon-based quantum dots and nanotubes. *Molecules* **2018**, *23*, 378.
(26) Arumugham, T.; Alagumuthu, M.; Amimodu, R. G.; Munusamy, S.; Iyer, S. K. A sustainable synthesis of green carbon quantum dot (CQD) from Catharanthus roseus (white flowering plant) leaves and investigation of its dual fluorescence responsive behavior in multi-ion detection and biological applications. *Sustainable Mater. Technol.* **2020**, *23*, e00138−e00149.
(27) Kong, W.; Wu, D.; Li, G.; Chen, X.; Gong, P.; Sun, Z.; Chen, G.; Xia, L.; You, J.; Wu, Y. A facile carbon dots based fluorescent probe for ultrasensitive detection of ascorbic acid in biological fluids via non-oxidation reduction strategy. *Talanta* **2017**, *165*, 677−684.
(28) Kumar, D.; Singh, K.; Verma, V.; Bhatti, H. S. Synthesis and Characterization of Carbon Quantum Dots from Orange Juice. *J. Bionanosci.* **2014**, *8*, 274−279.
(29) Liu, Y.; Liu, Y.; Park, M.; Park, S. J.; Zhang, Y.; Akanda, M. R.; Park, B. Y.; Kim, H. Y. Green synthesis of fluorescent carbon dots from carrot juice for in vitro cellular imaging. *Carbon Lett.* **2017**, *21*, 61−67.
(30) Kasibabu, B. S. B.; D'souza, S. L.; Jha, S.; Kailasa, S. K. Imaging of bacterial and fungal cells using fluorescent carbon dots prepared from carica papaya juice. *J. Fluorescence* **2015**, *25*, 803−810.
(31) Zhang, D.; Zhang, F.; Liao, Y.; Wang, F.; Liu, H. Carbon Quantum Dots from Pomelo Peel as Fluorescence Probes for "Turn-Off−On" High-Sensitivity Detection of Fe3+ and L-Cysteine. *Molecules* **2022**, *27*, 4099−4118.
(32) Ting, D.; Dong, N.; Fang, L.; Lu, J.; Bi, J.; Xiao, S.; Han, H. Correction to multisite inhibitors for enteric coronavirus: Antiviral cationic carbon dots based on curcumin. *ACS Appl. Nano Mater.* **2020**, *3*, 5451−5459.
(33) Bhatt, S.; Bhatt, M.; Kumar, A.; Vyas, G.; Gajaria, T.; Paul, P. Green route for synthesis of multifunctional fluorescent carbon dots from Tulsi leaves and its application as Cr (VI) sensors, bio-imaging and patterning agents. *Colloids Surf., B* **2018**, *167*, 126−133.
(34) Hoan, B. T.; Tam, P. D.; Pham, V. H. Green synthesis of highly luminescent carbon quantum dots from lemon juice. *J. Nanotechnol.* **2019**, No. 2852816.
(35) Zhao, Y.; Zhang, Y.; Liu, X.; Kong, H.; Wang, Y.; Qin, G.; Cao, P.; Song, X.; Yan, X.; Wang, Q.; Qu, H. Ror2 signaling regulates Golgi structure and transport through IFT20 for tumor invasiveness. *Sci. Rep.* **2017**, *7*, No. 1.
(36) Xiao, D.; Yuan, D.; He, H.; Lu, J. Microwave-assisted one-step green synthesis of amino-functionalized fluorescent carbon nitride dots from chitosan. *Luminescence* **2013**, *28*, 612−615.
(37) Liu, Y.; Xiao, N.; Gong, N.; Wang, H.; Shi, X.; Gu, W.; Ye, L. One-step microwave-assisted polyol synthesis of green luminescent carbon dots as optical nanoprobes. *Carbon* **2014**, *68*, 258−264.
(38) Gu, D.; Shang, S.; Yu, Q.; Shen, J. Green synthesis of nitrogen-doped carbon dots from lotus root for Hg(II) ions detection and cell imaging. *Appl. Surf. Sci.* **2016**, *390*, 38−42.
(39) Teng, X.; Ma, C.; Ge, C.; Yan, M.; Yang, J.; Zhang, Y.; Morais, P. C.; Bi, H. Green synthesis of nitrogen-doped carbon dots from konjac flour with "off−on" fluorescence by Fe3+ and l-lysine for bioimaging. *J. Mater. Chem. B* **2014**, *2*, 4631−4639.
(40) Shi, Y.; Li, C.; Liu, S.; Liu, Z.; Zhu, J.; Yang, J.; Hu, X. Facile synthesis of fluorescent carbon dots for determination of curcumin based on fluorescence resonance energy transfer. *RSC Adv.* **2015**, *5*, 64790−64796.
(41) Devi, P.; Saini, S.; Kim, K. H. The advanced role of carbon quantum dots in nanomedical applications. *Biosen. Bioelectron.* **2019**, *141*, No. 111158.
(42) Pires, N. R.; Santos, C. M.; Sousa, R. R.; Paula, R.; Cunha, P. L.; Feitosa, J. Novel and Fast Microwave-Assisted Synthesis of Carbon Quantum Dots from Raw Cashew Gum. *J. Braz. Chem. Soc.* **2015**, *26*, 1274−1282.
(43) Dias, C.; Vasimalai, N.; P Sárria, M.; Pinheiro, I.; Vilas-Boas, V.; Peixoto, J.; Espiña, B. Biocompatibility and Bioimaging Potential of Fruit-Based Carbon Dots. *Nanomaterials* **2019**, *9*, 199.
(44) Biswal, M.; Banerjee, A.; Deo, M.; Ogale, S. From dead leaves to high energy density supercapacitors. *Energy Environ. Sci* **2013**, *6*, 1249−1259.
(45) Sahu, S.; Behera, B.; Maiti, T. K.; Mohapatra, S. Simple one-step synthesis of highly luminescent carbon dots from orange juice: application as excellent bio-imaging agents. *Chem. Commun.* **2012**, *48*, 8835−8837.
(46) Nandi, R.; Mishra, S.; Maji, T. K.; Manna, K.; Kar, P.; Banerjee, S.; Dutta, S.; Sharma, S. K.; Lemmens, P.; Saha, K. D.; Pal, S. K. A novel nanohybrid for cancer theranostics: folate sensitized Fe $_2$ O $_3$ nanoparticles for colorectal cancer diagnosis and photodynamic therapy. *J. Mater. Chem. B* **2017**, *5*, 3927−3939.
(47) Mishra, S.; Manna, K.; Kayal, U.; Saha, M.; Chatterjee, S.; Chandra, D.; Hara, M.; Datta, S.; Bhaumik, A.; Saha, K. D. Folic acid-conjugated magnetic mesoporous silica nanoparticles loaded with quercetin: A theranostic approach for cancer management. *RSC Adv.* **2020**, *10*, 23148−23164.
(48) Rivas Aiello, M. B.; Azcárate, J. C.; Zelaya, E.; Gara, P. D.; Bosio, G. N.; Gensch, T.; Mártire, D. O. Photothermal therapy with silver nanoplates in HeLa cells studied by in situ fluorescence microscopy. *Biomater. Sci.* **2021**, *9*, 2608−2619.
(49) Mukherjee, T.; Soppina, V.; Ludovic, R.; Mély, Y.; Klymchenko, A. S.; Collot, M.; Kanvah, S. Live-cell imaging of the nucleolus and mapping mitochondrial viscosity with a dual function fluorescent probe. *Org. Biomol. Chem.* **2021**, *19*, 3389−3395.
(50) Jayaram, D. T.; Kumar, A.; Kippner, L. E.; Ho, P. Y.; Kemp, M. L.; Fan, Y.; Payne, C. K. TiO 2 nanoparticles generate superoxide and

https://doi.org/10.1021/acsomega.2c04964
ACS Omega 2023, 8, 4566−4577

alter gene expression in human lung cells. *RSC Adv.* **2019**, *9*, 25039−25047.
(51) Wang, Y. L.; Shen, Y.; Xu, J. P.; Han, K.; Zhou, Y.; Yang, S.; Yin, J. Y.; Min, D. L.; Hu, H. Y. Pterostilbene suppresses human endometrial cancer cells in vitro by down-regulating miR-663b. *Acta Pharmacol. Sin.* **2017**, *38*, 1394−1400.
(52) Pandey, S.; Patil, S.; Ballav, N.; Basu, S. Spatial targeting of Bcl-2 on endoplasmic reticulum and mitochondria in cancer cells by lipid nanoparticles. *J. Mater. Chem. B* **2020**, *8*, 4259−4266.
(53) Devaraj, P.; Kumari, P.; Aarti, C.; Renganathan, A. Synthesis and characterization of silver nanoparticles using cannonball leaves and their cytotoxic activity against MCF-7 cell line. *J. Nanotechnol.* **2013**, *2013*, 598328−598332.
(54) Choi, H.; Ko, S. J.; Choi, Y.; Joo, P.; Kim, T.; Lee, B. R.; Jung, J. W.; Choi, H. J.; Cha, M.; Jeong, J. R.; Hwang, I. W.; et al. Versatile surface plasmon resonance of carbon-dot-supported silver nanoparticles in polymer optoelectronic devices. *Nat. Photonics* **2013**, *7*, 732−738.
(55) Wang, W.; Damm, C.; Walter, J.; Nacken, T. J.; Peukert, W. Photobleaching and stabilization of carbon nanodots produced by solvothermal synthesis. *Physical Chemistry Chemical Physics* **2016**, *18*, 466−475.
(56) Liu, J.; Li, R.; Yang, B. Carbon dots: A new type of carbon-based nanomaterial with wide applications. *ACS Central Science* **2020**, *6*, 2179−2195.
(57) Wang, B.; Deng, A. J.; Li, Z. H.; Wang, N.; Qin, H. L. Syntheses and Structure−Activity Relationships in Growth Inhibition Activity against Human Cancer Cell Lines of 12 Substituted Berberine Derivatives. *Molecules* **2020**, *25*, 1871−1890.
(58) Zhang, C.; Sheng, J.; Li, G.; Zhao, L.; Wang, Y.; Yang, W.; Yao, X.; Sun, L.; Zhang, Z.; Cui, R. Effects of berberine and its derivatives on cancer: A systems pharmacology review. *Front. Pharmacol* **2020**, *10*, 1461−1470.
(59) Mohammadinejad, R.; Ahmadi, Z.; Tavakol, S.; Ashrafizadeh, M. Berberine as a potential autophagy modulator. *Journal of cellular physiology* **2019**, *234*, 14914−14926.
(60) Brattain, M. G.; Fine, W. D.; Khaled, F. M.; Thompson, J.; Brattain, D. E. Heterogeneity of malignant cells from a human colonic carcinoma. *Cancer Res.* **1981**, *41*, 1751−1756.
(61) Elmore, S. Apoptosis: a review of programmed cell death. *Toxicol. Pathol.* **2007**, *35*, 495−516.
(62) Brentnall, M.; Rodriguez-Menocal, L.; De Guevara, R. L.; Cepero, E.; Boise, L. H. Caspase-9, caspase-3 and caspase-7 have distinct roles during intrinsic apoptosis. *BMC Cell Biol.* **2013**, *14*, No. 32.
(63) Li, P.; Zhou, L.; Zhao, T.; Liu, X.; Zhang, P.; Liu, Y.; Zheng, X.; Li, Q. Caspase-9: structure, mechanisms and clinical application. *Oncotarget* **2017**, *8*, 23996−240008.
(64) Wang, C.; Youle, R. J. The role of mitochondria in apoptosis. *Ann. Rev. Gen.* **2009**, *43*, 95−118.
(65) Redza-Dutordoir, M.; Averill-Bates, D. A. Activation of apoptosis signalling pathways by reactive oxygen species. *Biochim. Biophys. Acta, Mol. Cell Res.* **1863**, *2016*, 2977−2992.
(66) Shamas-Din, A.; Kale, J.; Leber, B.; Andrews, D. W. Mechanisms of action of Bcl-2 family proteins. *Cold Spring Harbor Perspect. Biol.* **2013**, *5*, No. a008714.
(67) Xie, Y. H.; Chen, Y. X.; Fang, J. Y. Comprehensive review of targeted therapy for colorectal cancer. *Signal Transduction and Targeted Ther.* **2020**, *5*, No. 22.
(68) Pugazhenthi, S.; Nesterova, A.; Sable, C.; Heidenreich, K. A.; Boxer, L. M.; Heasley, L. E.; Reusch, J.E.B. Akt/protein kinase B up-regulates Bcl-2 expression through cAMP-response element-binding protein. *J. Biol. Chem.* **2000**, *275*, 10761−10766.
(69) Redondo-Blanco, S.; Fernández, J.; Gutiérrez-del-Río, I.; Villar, C. J.; Lombó, F. New insights toward colorectal cancer chemotherapy using natural bioactive compounds. *Front. Pharmacol.* **2017**, *8*, 109.
(70) Brooks, C. L.; Gu, W. New insights into p53 activation. *Cell Res.* **2010**, *20*, 614−621.
(71) Hardwick, J. M.; Soane, L. Multiple functions of BCL-2 family proteins. *Cold Spring Harbor Perspect. Biol.* **2013**, *5*, No. a008722.
(72) Ozaki, T.; Nakagawara, A. Role of p53 in cell death and human cancers. *Cancers* **2011**, *3*, 994−1013.
(73) Zorov, D. B.; Juhaszova, M.; Sollott, S. J. Mitochondrial reactive oxygen species (ROS) and ROS-induced ROS release. *Physiol. Rev.* **2014**, *94*, 909−950.
(74) Fulda, S.; Debatin, K. M. Extrinsic versus intrinsic apoptosis pathways in anticancer chemotherapy. *Oncogene* **2006**, *25*, 4798−4811.

https://doi.org/10.1021/acsomega.2c04964
ACS Omega 2023, 8, 4566−4577